



RESEARCH ARTICLE

Performance of a two-body wave energy converter with an annular heave plate

Raj Tamakuwala^{1,#}, Muhammad Usman^{2,#} , Nathan Tom³ and Hassan Masoud² 

¹Department of Mechanical and Aerospace Engineering, Michigan Technological University, Houghton, MI, USA

²Department of Mechanical Engineering, Clemson University, Clemson, SC, USA

³National Renewable Energy Laboratory, Golden, CO, USA

Corresponding author: Hassan Masoud; Email: hmasoud@clemson.edu

Received: 21 March 2025; **Revised:** 5 July 2025; **Accepted:** 18 August 2025

Keywords: wave energy conversion; two-body point absorber; regular waves

Abstract

We theoretically examine the performance of a two-body wave energy converter (WEC) featuring a floating sphere and a submerged annular heave plate, connected by a power take-off (PTO) system. Utilising linear wave theory, we derive the system's frequency-domain response to regular plane waves and analyse the impact of varying disk porosity on power generation. Our results suggest that annular disks can enhance power extraction efficiency in various cases compared with solid heave plates. Additionally, permeable plates can broaden operational conditions by reducing oscillation amplitudes and decreasing the mechanical strain on the PTO system without substantially compromising the power conversion efficiency. Overall, our findings provide valuable insights for optimising WEC designs to improve energy capture, emphasising the potential hydrodynamic advantages of using porous reaction bodies.

Impact Statement

This study advances the understanding of fundamental flow physics in wave energy conversion by analysing the hydrodynamics of a two-body wave energy converter (WEC) with an annular heave plate. Using linear wave theory, we investigate how varying the disk porosity influences power extraction efficiency and mechanical loading. The study provides insight into the interplay between hydrodynamic forces and structural response, particularly the influence of added mass and radiation damping on energy transfer. Our findings reveal that porous heave plates can enhance energy capture while mitigating excessive oscillations, thus improving system stability.

The translational impact of this research lies in its contribution to the design and optimisation of next-generation wave energy technologies. By demonstrating that annular heave plates can broaden operational conditions without significant efficiency loss, this work informs the development of more resilient and efficient WECs. The findings have direct implications for renewable energy generation, offshore infrastructure and sustainable marine technologies, contributing to the expansion of wave energy as a viable power source for remote and coastal communities.

[#] Authors of equal contribution.

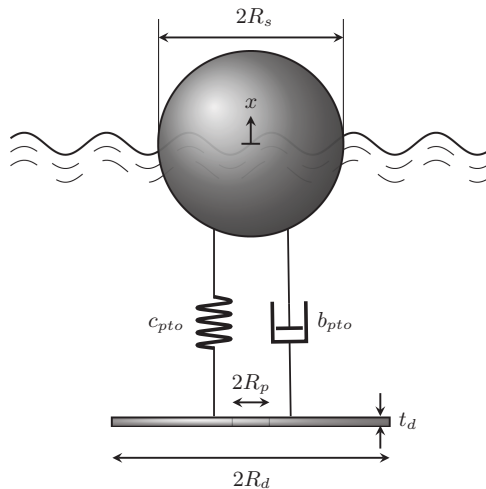


Figure 1. Schematics of our two-body point-absorber WEC consisting of a floating sphere of radius R_s and a submerged annular disk of inner radius R_p and outer radius R_d . The sphere and disk are connected together by a spring of constant c_{pto} and a dashpot with a damping coefficient of b_{pto} .

1. Introduction

Wave energy conversion has strong potential as a sustainable and environmentally friendly source of renewable energy (Drew *et al.*, 2009; Falcao, 2010; López *et al.*, 2013; Sheng, 2019; Soares *et al.*, 2012; Guo & Ringwood, 2021b; Clemente *et al.*, 2021; Guo *et al.*, 2022; Li *et al.*, 2021). Unlike fossil fuels, wave energy produces no greenhouse gas emissions and can be developed with minimal impact on marine ecosystems, with some systems even providing artificial habitats. Although not yet widely deployed, continued research and development could enable broader adoption and help reduce reliance on non-renewable energy sources. Wave energy can also support various coastal and offshore applications, such as desalination, renewable power for offshore industries and electricity for remote coastal or island communities. It can power floating sensors, underwater vehicles for ocean monitoring and aquaculture operations that require a steady energy supply for feeding, filtration and monitoring. By complementing other renewable sources, wave energy conversion can contribute to a more resilient and sustainable energy portfolio. Despite this strong potential, the widespread adoption of wave energy conversion faces significant challenges. These include high capital and maintenance costs, the need for robust designs to survive harsh marine environments, difficulties in long-term device reliability and the variable nature of wave energy, which can complicate consistent power delivery and grid integration. These drawbacks have historically limited the deployment of market-ready wave energy devices, despite substantial global investment and research efforts.

When deployed in relatively moderate to deep waters, wave energy converters (WECs) at the utility and even powering-the-blue-economy scales can be viewed generally as two-body assemblies. Such systems consist of a surface-piercing (or near-surface) body, which is the main mover excited primarily by the incident waves, and a deeper subsurface (reaction) body that is designed to provide the greatest relative motion for maximum power capture (see figure 1). The most common reaction body used is the heave plate and its associated variants. The heave plate has been chosen, for the most part, because its added mass-to-volume ratio is one of the best for bodies oscillating in an infinite fluid medium, which is a reasonable assumption for reaction bodies deeper than 20 m below the water surface. While some progress has been made to date in optimising the shape of floating bodies to maximise power capture (Esmaeilzadeh & Alam, 2019; Garcia-Teruel & Forehand, 2021; Goggins & Finnegan, 2014; Guo & Ringwood, 2021a), efforts to achieve more efficient power extraction by adjusting the hydrodynamic response of subsurface bodies remain limited.

A practical way to influence the hydrodynamics of heave plates is to alter their permeability, e.g. through perforation (Hamilton *et al.*, 2021; Rosenberg & Mundon, 2016). However, little is known about the comparative performance of WECs with porous heave plates versus traditional solid reaction plates. To help fill this gap, here, we theoretically analyse the performance of a two-body WEC consisting of a spherical float linked to a heave plate in the form of an annular disk via a power take-off (PTO) system. The annular disk represents perhaps the simplest perforated disk with only a single hole in the middle. We apply the linear wave theory to calculate the WEC's frequency-domain response to regular plane waves, assuming small-amplitude harmonic oscillations. Specifically, we examine how varying the disk porosity affects the performance of the WEC under incident waves of different frequencies. Our calculations reveal numerous scenarios where using annular disks instead of solid ones can enhance power generation. We also find that permeable plates can broaden the operational conditions for WECs by lowering the amplitude of oscillations without sacrificing power conversion efficiency. Furthermore, our results indicate that annular plates may lower the strain on the PTO system with minimal impact on converted power.

In what follows, we first describe the problem statement and our solution (§ 2). The results of our calculations are presented and discussed next (§ 3). A short summary and concluding remarks are given at the end (§ 4) and supplemental information is provided in Appendices A, B and C.

2. Problem statement and solution

We seek to calculate the power extracted from regular waves by a two-body WEC consisting of (i) a floating spherical buoy, (ii) a submerged annular disk acting as a heave plate and (iii) a PTO system connecting the two bodies by a spring and damper with adjustable coefficients (see figure 1). Suppose (i) the water depth is infinite, (ii) the thickness of the disk is negligible hydrodynamically, (iii) the wave amplitude is sufficiently small, compared with the characteristic dimensions of the buoy and disk, to allow the system to be reasonably approximated as linear, (iv) the spherical buoy is half-submerged when the whole assembly is at rest, (v) the viscous damping of the floating body and the radiation damping of the submerged body can be ignored, (vi) the hydrodynamic coupling between the floating and submerged bodies is very weak, (vii) the motion of both the buoy and disk is restricted to heave in the x direction and (viii) the PTO system has negligible mass.

Under these typical conditions (Beatty *et al.*, 2015; Falnes, 1999; Liang & Zuo, 2017; Wu *et al.*, 2014), the dynamics of the coupled system is governed by

$$f_s = (m_s + a_s)\ddot{x}_s + b_s\dot{x}_s + b_{pto}(\dot{x}_s - \dot{x}_d) + c_{pto}(x_s - x_d) + c_s x_s, \quad (2.1)$$

$$f_d = (m_d + a_d)\ddot{x}_d + b_d\dot{x}_d + b_{pto}(\dot{x}_d - \dot{x}_s) + c_{pto}(x_d - x_s), \quad (2.2)$$

where f , m , \ddot{x} , \dot{x} , x , a and b represent the excitation force, mass, acceleration, velocity, displacement, and added mass and damping coefficients, respectively, with variables belonging to the sphere, disk and PTO being distinguished by the subscripts s , d and pto , respectively. Also, c_s and c_{pto} denote the hydrostatic spring coefficient of the buoy and the spring constant of the PTO system, respectively.

Our goal is to solve the above coupled linear ordinary differential equations and use the solution to determine the power converted by the WEC system. In the first step, it is mathematically convenient to express the variables of interest as real parts of complex quantities, i.e.

$$f_s = \text{Re} [F_s \exp(i \omega t)], \quad (2.3)$$

$$f_d = \text{Re} [F_d \exp(i \omega t)], \quad (2.4)$$

$$\dot{x}_s = \text{Re} [\dot{X}_s \exp(i \omega t)], \quad (2.5)$$

$$\dot{x}_d = \text{Re} [\dot{X}_d \exp(i \omega t)], \quad (2.6)$$

$$\dot{x}_r = \dot{x}_s - \dot{x}_d = \operatorname{Re} \left[\dot{X}_r \exp(i \omega t) \right], \quad (2.7)$$

where ω and t represent the angular frequency of the incident wave and time, respectively, and $i^2 = -1$. Next, we can rewrite (2.1) and (2.2) in the frequency domain as

$$F_s = Z_s \dot{X}_s + Z_{pto} \dot{X}_r, \quad (2.8)$$

$$F_d = Z_d \dot{X}_d - Z_{pto} \dot{X}_r, \quad (2.9)$$

where

$$Z_s = b_s + i \omega \left(m_s + a_s - \frac{c_s}{\omega^2} \right), \quad (2.10)$$

$$Z_d = b_d + i \omega (m_d + a_d), \quad (2.11)$$

$$Z_{pto} = b_{pto} + \frac{c_{pto}}{i \omega}. \quad (2.12)$$

Taking the difference of (2.8) and (2.9), after some rearrangements, we arrive at the following relation for the relative velocity of the buoy and disk:

$$\dot{X}_r = \frac{F_0}{Z_i + Z_{pto}}, \quad (2.13)$$

where

$$Z_i = \frac{Z_s Z_d}{Z_s + Z_d}, \quad (2.14)$$

$$F_0 = \left(\frac{Z_d}{Z_s + Z_d} \right) F_s - \left(\frac{Z_s}{Z_s + Z_d} \right) F_d. \quad (2.15)$$

With \dot{X}_r known, the velocity of the sphere and disk can be obtained through, respectively,

$$\dot{X}_s = \frac{F_s - Z_{pto} \dot{X}_r}{Z_s}, \quad (2.16)$$

$$\dot{X}_d = \frac{F_d + Z_{pto} \dot{X}_r}{Z_d}. \quad (2.17)$$

The average power converted by the PTO system during one period of oscillations T is calculated from

$$\begin{aligned} \bar{P} &= \frac{1}{T} \int_0^T (b_{pto} \dot{x}_r + c_{pto} x_r) \dot{x}_r dt = \frac{1}{T} \int_0^T b_{pto} \dot{x}_r^2 dt \\ &= \frac{1}{2} b_{pto} |\dot{X}_r|^2 = \frac{1}{2} b_{pto} \left| \frac{F_0}{Z_i + Z_{pto}} \right|^2. \end{aligned} \quad (2.18)$$

Multiplying (2.1) and (2.2) by \dot{x}_s and \dot{x}_d , respectively, and adding, gives

$$\begin{aligned} f_s \dot{x}_s + f_d \dot{x}_d &= (m_s + a_s) \ddot{x}_s \dot{x}_s + b_s \dot{x}_s^2 + b_{pto} (\dot{x}_s - \dot{x}_d) \dot{x}_s + c_{pto} (x_s - x_d) \dot{x}_s + c_s x_s \dot{x}_s \\ &\quad + (m_d + a_d) \ddot{x}_d \dot{x}_d + b_d \dot{x}_d^2 + b_{pto} (\dot{x}_d - \dot{x}_s) \dot{x}_d + c_{pto} (x_d - x_s) \dot{x}_d. \end{aligned} \quad (2.19)$$

Combining the PTO terms, we have

$$b_{pto} (\dot{x}_s - \dot{x}_d) \dot{x}_s + b_{pto} (\dot{x}_d - \dot{x}_s) \dot{x}_d = b_{pto} (\dot{x}_s^2 + \dot{x}_d^2 - 2 \dot{x}_s \dot{x}_d) = b_{pto} \dot{x}_r^2. \quad (2.20)$$

Over one oscillation period, the time average of the inertial terms vanishes, i.e.

$$\int_0^T \ddot{x}_s \dot{x}_s dt = \int_0^T \ddot{x}_d \dot{x}_d dt = 0. \quad (2.21)$$

Also, the spring terms are conservative and thus do not contribute to the net power. Therefore, after averaging over a cycle, the mean converted power is

$$\bar{P} = \underbrace{\frac{1}{T} \int_0^T f_s \dot{x}_s dt}_{\bar{P}_s^e} + \underbrace{\frac{1}{T} \int_0^T f_d \dot{x}_d dt}_{\bar{P}_d^e} - \underbrace{\frac{1}{T} \int_0^T b_s \dot{x}_s^2 dt}_{\bar{P}_s^d} - \underbrace{\frac{1}{T} \int_0^T b_d \dot{x}_d^2 dt}_{\bar{P}_d^d}, \quad (2.22)$$

where \bar{P}_s^e and \bar{P}_d^e are the input powers due to the excitation forces exerted on the sphere and disk, respectively, and \bar{P}_s^d and \bar{P}_d^d are the power dissipated due to their motions. For a given F_0 and Z_i , it can be shown (see, e.g. Falnes, 1999) that \bar{P} is maximum when Z_{pto} is equal to the complex conjugate of Z_i (denoted by Z_i^*), leading to

$$\bar{P}_{max} = \frac{|F_0|^2}{8 \operatorname{Re}(Z_i)}, \quad (2.23)$$

where $\operatorname{Re}(Z_i)$ denotes the real part of Z_i . However, if Z_{pto} is restricted to be real (i.e. the spring constant of the PTO systems is set to zero), then the maximum power is extracted when b_{pto} is equal to the magnitude of Z_i (denoted by $|Z_i|$), resulting in

$$\bar{P}_{max}^{res} = \frac{|F_0|^2}{4 [\operatorname{Re}(Z_i) + |Z_i|]}. \quad (2.24)$$

In practice, PTO systems can maintain near-optimal conditions by actively adjusting the resistive damping through various control strategies.

To evaluate the maximum power in either case, we need first to determine F_s , F_d , c_s , a_s , b_s , a_d and b_d . The excitation forces on the sphere and disk are related to the corresponding radiation damping of these objects through the Haskind relation (see, e.g. Falnes, 2002). For the sphere, this means

$$F_s = |F_s| = \sqrt{8Q \left(\frac{\lambda}{2\pi} \right) b_s}, \quad (2.25)$$

where $Q = \rho g^2 A^2 / 4 \omega$, $\lambda = 2\pi g / \omega^2$ and A are the power flux, wavelength and amplitude of the incident wave, respectively, with ρ being the density of water and g being the gravitational acceleration. Also, for the disk, the reciprocity relation between the radiation resistance and the excitation force demands F_d to vanish since the radiation damping of the disk is negligible. To obtain explicit expressions for the maximum extracted powers, we first substitute the relations for F_s and F_d into (2.15). We then insert the result into (2.23) and (2.24) and use the definition of Z_i from (2.14) to obtain

$$\bar{P}_{max} = Q \left(\frac{\lambda}{2\pi} \right) \left\{ 1 + \left(\frac{b_d}{b_s} \right) \left[\frac{b_s^2 + \omega^2 (m_s + a_s - c_s / \omega^2)^2}{b_d^2 + \omega^2 (m_d + a_d)^2} \right] \right\}^{-1}, \quad (2.26)$$

$$\begin{aligned} \frac{\bar{P}_{max}^{res}}{2 \bar{P}_{max}} &= \left\{ 1 + \sqrt{1 + \left[\frac{\operatorname{Im}(Z_i)}{\operatorname{Re}(Z_i)} \right]^2} \right\}^{-1} \\ &= \left(1 + \sqrt{1 + \left\{ \frac{(m_d + a_d) + \left[\frac{b_d^2 + \omega^2 (m_d + a_d)^2}{b_s^2 + \omega^2 (m_s + a_s - c_s / \omega^2)^2} \right] (m_s + a_s - c_s / \omega^2)}{\frac{b_d}{\omega} + \left[\frac{b_d^2 + \omega^2 (m_d + a_d)^2}{b_s^2 + \omega^2 (m_s + a_s - c_s / \omega^2)^2} \right] \left(\frac{b_s}{\omega} \right)} \right\}^2} \right)^{-1}, \end{aligned} \quad (2.27)$$

where $\operatorname{Im}(Z_i)$ denotes the imaginary part of Z_i . Additionally, given that the sphere is half-submerged at rest, it is straightforward to show that the linearised spring coefficient due to changes in the buoyancy of the sphere takes the form of

$$c_s = \rho g \pi R_s^2, \quad (2.28)$$

Table 1. Incident wave and WEC properties

<i>A</i>	<i>T</i>	ρ	<i>g</i>	<i>R_s</i>	<i>R_d/R_s</i>	<i>R_p/R_d</i>	<i>t_d/R_d</i>
1 m	5–15 s	998 kg m ^{−3}	9.81 m s ^{−2}	10 m	0.5–1.5	0.001–0.5	0.01

where R_s represents the radius of the sphere, and that

$$m_s + m_d = \rho \pi \left[\frac{2R_s^3}{3} + t_d (R_d^2 - R_p^2) \right], \tag{2.29}$$

with R_d and R_p denoting, respectively, the outer and inner radii of the disk and t_d representing its thickness (see also figure 1).

We use the expressions derived by Hulme (1982) using the linear wave theory to compute a_s and b_s . We also use the formulation developed by Usman & Masoud (2025), which is based on the linearised Navier–Stokes equations combined with perturbation theory and the reciprocal theorem, to obtain a_d and b_d . To maintain clarity and a seamless flow of information in the main text, the exact equations used and the behaviour of the calculated coefficients are provided in Appendices A and B.

While the assumptions made here are consistent with the practical parameter range described in the following section, relaxing these conditions – for example, by considering larger wave amplitudes or stronger hydrodynamic coupling – would require accounting for nonlinear and boundary effects. These factors could modify the resonance behaviour, optimal PTO settings and predicted power performance, motivating future studies using detailed numerical simulations or experimental measurements.

3. Results and discussion

We set the properties and dimensions of our WEC to be consistent with the assumptions outlined at the beginning of § 2 and to align closely with those of Reference Model 3 (Neary *et al.*, 2014), a benchmark two-body point-absorber WEC designed by the U.S. Department of Energy’s national laboratories to facilitate standardised evaluation of the performance and cost of various marine hydrokinetic technologies. Table 1 lists our chosen parameters. Additionally, we assume that both the float and the reaction plate are made of steel with a density of $\rho_{steel} = 7800 \text{ kg m}^{-3}$. Note that the mass of the buoy is calculated from (2.29), eliminating the need to explicitly specify the thickness of the spherical shell. These selections ensure that our study covers a range of practical scenarios of current interest. To analyse the performance of our WEC, we focus on the case where the PTO system exerts only a resistive force, achieved by setting the spring constant of the PTO to zero. This simplification avoids the complications of negative spring constants, which could arise if no restrictions are placed on c_{pto} . In this scenario, the spring’s restoring force acts in the same direction as its displacement rather than opposing it, which is generally destabilising. In our model, the mean tension in the PTO lines is maintained by a mechanical mechanism that allows the system to oscillate around its mean position. However, in practice, a spring term is often included to compensate for weight discrepancies.

Figures 2, 3, 4 and 5 present the outcomes of our calculations. Specifically, figure 2 shows the maximum average extracted power (\bar{P}_{max}^{res}), the associated amplitude of the relative displacement between the buoy and the disk ($|X_r|$) and the damping coefficient of the PTO (b_{pto}) versus the wave period (T) for disk outer radius to sphere radius ratios of $R_d/R_s = 1/2, 1, 3/2$ and 2 (represented by the blue, black, red and green curves, respectively). In this figure, the left, middle and right columns correspond to the ratios of the inner-to-outer radius of the disk $R_p/R_d = 10^{-2}, 10^{-1}$ and $1/2$, respectively. Figure 3 illustrates these same variables but plotted against R_p/R_d , with the left, middle and right columns corresponding to $T = 5, 10$ and 15 s , respectively. Figure 4 normalises these variables by their respective values against the baseline scenario of solid disk with $R_p = 0$ (distinguished by the subscript 0), and figure 5 further explores the normalised variables across different wave periods. This normalisation reveals the efficiency gains or losses attributed to the annular design.

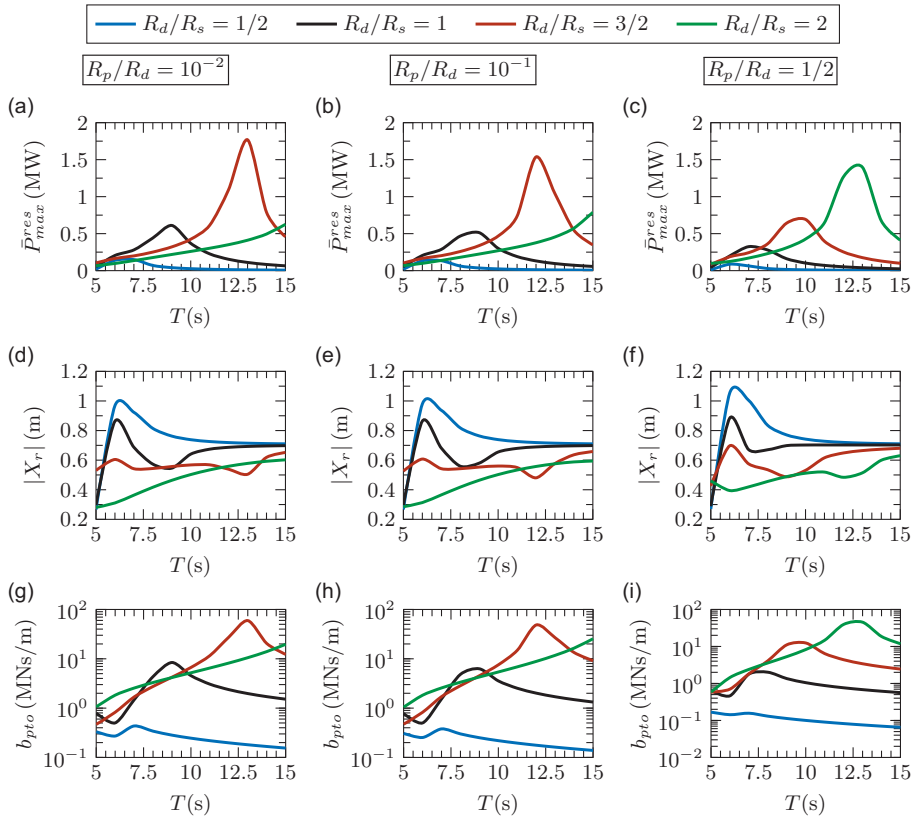


Figure 2. Plots of (a–c) the maximum average extracted power when $c_{pto} = 0$ (denoted by \bar{P}_{max}^{res}), the corresponding (d–f) amplitude of the relative displacement between the buoy and the disk (denoted by $|X_r|$) and (g–i) the damping coefficient of the PTO (denoted by b_{pto}) versus the wave period (denoted by T) for the WEC parameters listed in table 1 and the disk outer radius to sphere radius ratio of $R_d/R_s = 1/2, 1, 3/2$ and 2. The left, middle and right columns are for $R_p/R_d = 10^{-2}, 10^{-1}$ and $1/2$, respectively.

Given Eqs. (2.26)–(2.29) and the asymptotic behaviours of the added mass and damping coefficients of the sphere and the disk (see Appendices A and B), it can be deduced that \bar{P}_{max}^{res} approaches zero in the extreme limits of $T \rightarrow 0$ and $T \rightarrow \infty$ (see also (C.1) of Appendix C). Consequently, the extracted power is expected to peak at an intermediate wave period. This expectation is confirmed by our results, although the wave period at which \bar{P}_{max}^{res} peaks lies outside $5 \text{ s} \leq T \leq 15 \text{ s}$ for $R_d/R_s = 2$ when the disk's pore size is not large enough (see the first row of figure 2). We find that, within the range of parameters considered, decreasing the size of the reaction plate relative to the float (i.e. lowering R_d/R_s) shifts the \bar{P}_{max}^{res} versus T curves to the left. Increasing the disk's porosity produces the same effect, hence the appearance of the green curve's peak for $R_d/R_s = 2$ and $R_p/R_d = 1/2$ in figure 2c. Due to these shifts, at a given T and $R_d/R_s = 2$, the introduction of a hole in the centre of a solid reaction disk can either enhance or reduce power extraction (see the first rows of figures 4 and 5). Notably, the order of magnitude of \bar{P}_{max}^{res} at the peak points is approximated well by the corresponding Q ($\lambda/2\pi$), which is the prefactor in (2.26) (see also (C.1) of Appendix C).

Regarding the variations of the amplitude of the relative displacement, the following observations can be made for $R_p/R_d = 10^{-2}$ (see figure 2d). For $R_d/R_s = 1/2$, $|X_r|$ increases from the starting point of around 0.3 m at $T = 5 \text{ s}$ before reaching a peak of slightly above 1 m at about $T = 6 \text{ s}$, and then gradually decreases and plateaus around 0.7 m when T approaches 15 s (see the blue curve). A very similar trend is

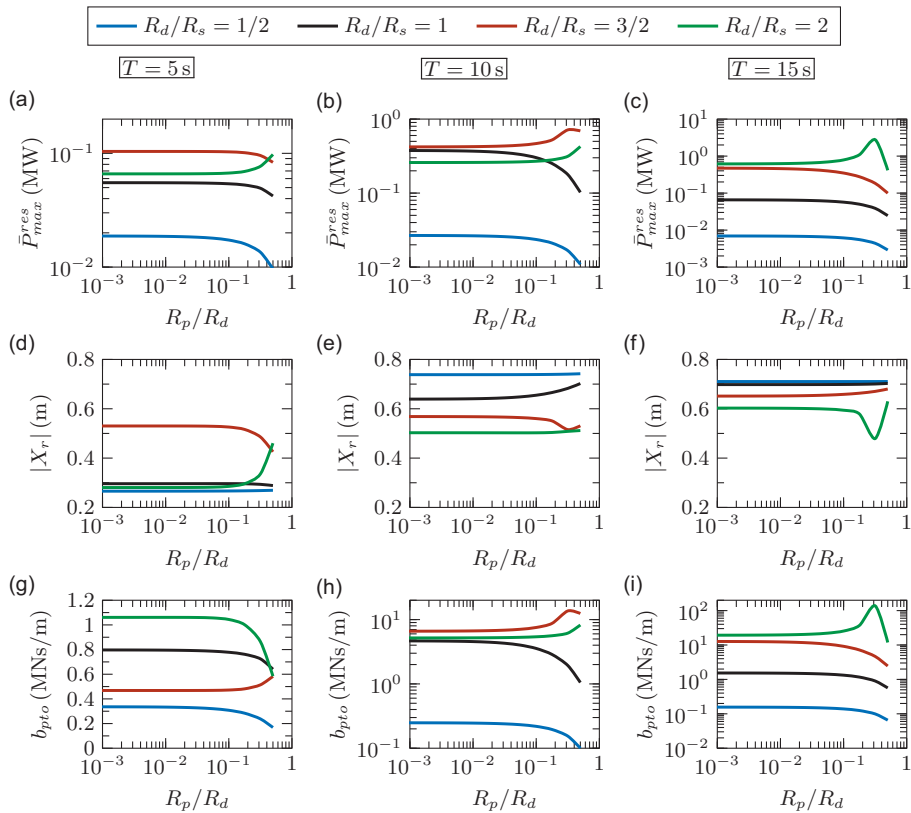


Figure 3. Plots of (a–c) the maximum average extracted power when $c_{pto} = 0$ (denoted by \bar{P}_{max}^{res}), the corresponding (d–f) amplitude of the relative displacement between the buoy and the disk (denoted by $|X_r|$) and (g–i) the damping coefficient of the PTO (denoted by b_{pto}) versus the ratio of the inner-to-outer radius of the disk (i.e. R_p/R_d) for the WEC parameters listed in table 1 and the disk outer radius to sphere radius ratio of $R_d/R_s = 1/2, 1, 3/2$ and 2 . The left, middle and right columns are for $T = 5, 10$ and 15 s, respectively.

observed for $R_d/R_s = 1$ (see the black curve), whereas, for $R_d/R_s = 3/2$, the amplitude starts above 0.5 m and generally increases with increasing T to just below 0.7 m at the end, while exhibiting minor fluctuations (see the red curve). For the highest ratio of disk-to-sphere radius, $|X_r|$ rises from approximately 0.3 to 0.6 m during the interval of wave periods examined (see the green curve). The abovementioned patterns are closely followed for $R_p/R_d = 10^{-1}$ (see figure 2e). The described behaviours are replicated, although with some deviations, for $R_p/R_d = 1/2$, as well (see figure 2f). Overall, we see that, in most cases, the amplitude of the relative displacement is lower for disks with larger outer radius. We also see that, depending on the ratio R_d/R_s and the period of the wave, increasing the porosity of the disk may increase or reduce $|X_r|$ (see the middle rows figures 4 and 5). Nevertheless, the order of magnitude of $|X_r|$ remains comparable to the wave amplitude A (see (C.2) of Appendix C). Lastly, we find that the peaks of \bar{P}_{max}^{res} correspond to the troughs of $|X_r|$, except for $R_d/R_s = 1/2$, in which case both quantities peak at the same wave period (see the first and second rows of figure 2). This behaviour partly stems from the difference in the last terms inside the curly brackets in (C.1) and (C.2) of Appendix C.

As for the changes in the resistance coefficient of the PTO, the general trend of the curves shown in the last rows of figures 2, 3, 4 and 5 resembles those of the plots illustrated in the first rows of the same figures for the captured power. Notable differences, however, are seen in the range $5 \text{ s} \leq T \leq 7 \text{ s}$. Also, while the peaks of \bar{P}_{max}^{res} and b_{pto} line up closely for $R_d/R_s = 1, 3/2$ and 2 , the peaks of \bar{P}_{max}^{res} for the smallest disk radius are aligned with local minima for b_{pto} (compare the curves in the first row of

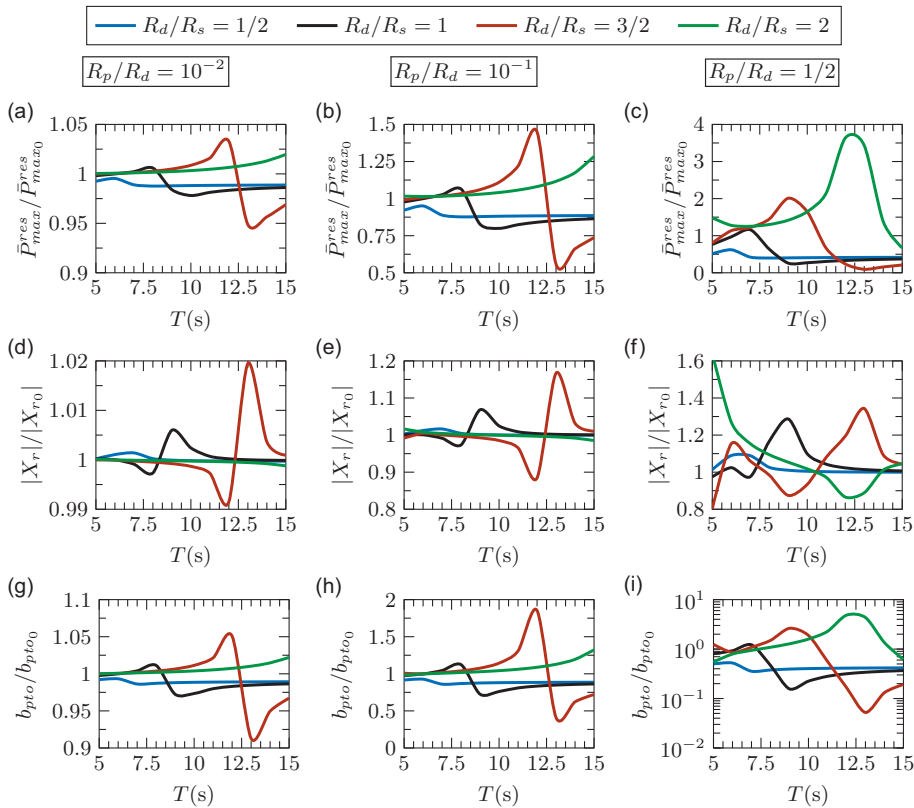


Figure 4. Plots of (a–c) \bar{P}_{max}^{res} , (d–f) $|X_r|$ and (g–i) b_{pto} normalised by their corresponding values for a solid disk with $R_p = 0$ (distinguished by the subscript 0) versus T for the WEC parameters listed in table 1 and $R_d/R_s = 1/2, 1, 3/2$ and 2. The left, middle and right columns are for $R_p/R_d = 10^{-2}, 10^{-1}$ and $1/2$, respectively.

figure 2 with the same curves in the last row of this figure). Last but not least, we find that the maximum values of b_{pto} roughly scale with $\rho R_d^3 \omega$ (see (C.3) of Appendix C).

4. Summary

We theoretically analysed the performance of a WEC consisting of a floating sphere and a submerged annular heave plate coupled through a purely resistive PTO system. We examined various scenarios by adjusting the disk's porosity and the ratio of the disk's outer radius to the sphere's radius over a range of realistic wave periods, focusing on the implications for power extraction efficiency and operational conditions. Our analysis revealed a complex interplay between wave period, geometric configurations and disk porosity in optimising WEC performance. Notably, we found that annular disks can significantly improve power capture efficiency compared with solid disks, particularly for certain ratios of disk-to-sphere radius. This enhancement, often accompanied by a reduced amplitude of oscillation for the relative motion between the float and heave plate, may, however, increase the demands on the PTO system, as evidenced by higher normalised damping coefficients. These findings underscore the necessity of balancing power capture with managing mechanical stress across varying sea states to ensure efficient and resilient WEC operation.

In conclusion, the annular disk design offers substantial advantages in power conversion efficiency, highlighting the importance of optimising the reaction plate's dimensions and porosity. While these benefits must be weighed against the increased mechanical complexity and stress on the system, the optimal parameters identified in this study provide valuable insights for designing more effective

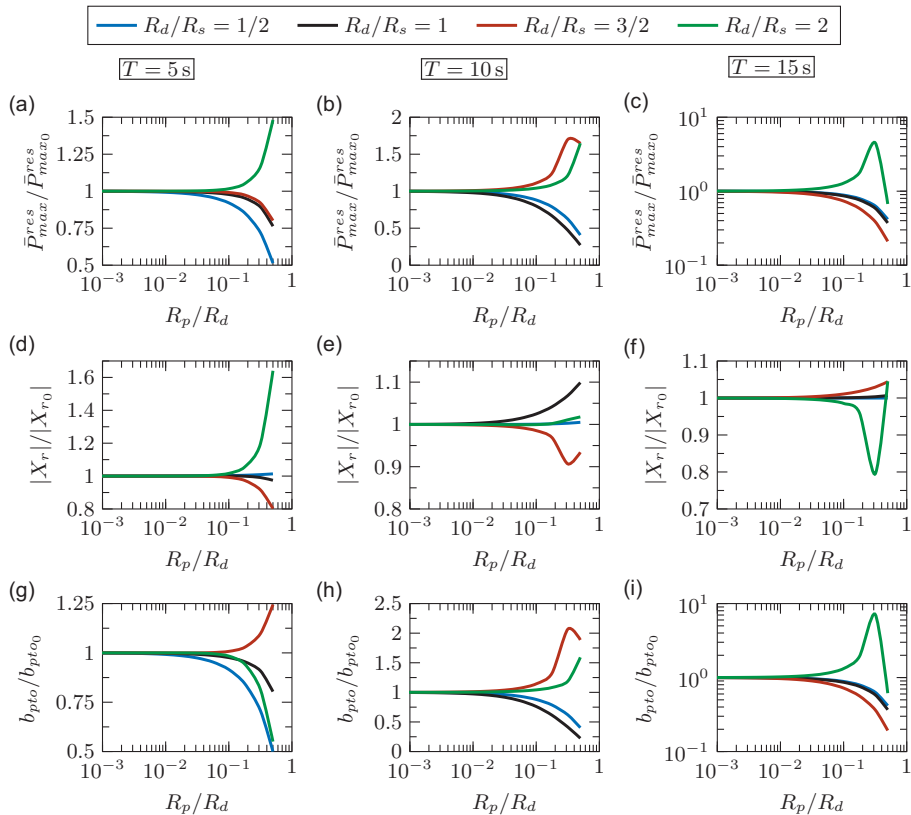


Figure 5. Plots of (a–c) \bar{P}_{max}^{res} , (d–f) $|X_r|$ and (g–i) b_{pto} normalised by their corresponding values for a solid disk with $R_p = 0$ (distinguished by the subscript 0) versus R_p/R_d for the WEC parameters listed in table 1 and $R_d/R_s = 1/2, 1, 3/2$ and 2. The left, middle and right columns are for $T = 5, 10$ and 15 s, respectively.

WECs. These findings also provide a clear theoretical foundation for future wave tank experiments and prototype field trials to validate the predicted power performance and guide practical design improvements. Future research should focus on the long-term durability and economic feasibility of these designs under real-world conditions. Additionally, it is crucial to experimentally verify the theoretical predictions made in our study to identify any deviations from assumptions and facilitate the refinement and extension of the model for practical applications. Such validation could be carried out through scale-model wave tank experiments or prototype field tests that measure the relative motion between the buoy and the disk, hydrodynamic forces, PTO damping characteristics and energy extraction efficiency under controlled sea states, enabling direct comparison with the frequency-domain predictions developed here. Moreover, our work paves the way for further investigations into more advanced scenarios involving perforated disks with multiple pores. Of particular interest would be determining the optimum pore size and distribution for a fixed total porosity. Understanding the hydrodynamic effects of various pore configurations is essential for developing more efficient and robust porous reaction plates.

Acknowledgements. We thank Dr. Salman Husain for stimulating discussions and for his feedback on the manuscript.

Funding statement. Financial support from the Water Power Technologies Office of the U.S. Department of Energy through a Seeding grant is gratefully acknowledged.

Competing interests. The authors declare no conflict of interest.

Appendix A. Added mass and radiation damping of a half-submerged sphere

Following Hulme (1982), the added mass a_s and radiation damping b_s coefficients of a half-submerged sphere can be expressed as

$$\begin{aligned} \frac{a_s}{\rho R_s^3} + i \frac{b_s}{\rho R_s^3 \omega} &= a_s^* + i b_s^* \\ &= -2\pi\beta_0 \left\{ \frac{1}{2} + \Lambda \sum_{m=0}^{\infty} \frac{(-\Lambda)^m}{m!} [\Psi(n) + i\pi - \ln \Lambda] \mathcal{I}(1, m) - \frac{\partial \mathcal{I}}{\partial \sigma} \bigg|_{\substack{\nu=1 \\ \sigma=m}} \right. \\ &\quad \left. + \sum_{n=1}^{\infty} \beta_n \left[\frac{\Lambda}{2n} \mathcal{I}(1, 2n-1) + \mathcal{I}(1, 2n) \right] \right\}, \end{aligned} \quad (\text{A.1})$$

where

$$\Lambda = \omega^2 R_s / g, \quad (\text{A.2})$$

$$\Psi(n) = \begin{cases} -\gamma & \text{if } n = 0, \\ -\gamma + \sum_{k=1}^n \frac{1}{k} & \text{if } n \neq 0, \end{cases} \quad (\text{A.3})$$

$$\mathcal{I}(\nu, \sigma) = \frac{2 \left[A(\nu, \sigma)^2 \sin(\pi \nu/2) \cos(\pi \sigma/2) - \cos(\pi \nu/2) \sin(\pi \sigma/2) \right]}{\pi A(\nu, \sigma) (\nu - \sigma) (\nu + \sigma + 1)}, \quad (\text{A.4})$$

$$A(\nu, \sigma) = \frac{\Gamma(\nu/2 + 1) \Gamma(\sigma/2 + 1/2)}{\Gamma(\nu/2 + 1/2) \Gamma(\sigma/2 + 1)}, \quad (\text{A.5})$$

with γ being the Euler–Mascheroni constant and Γ representing the gamma function. Here, the coefficients β_n are calculated from

$$\beta_0 = \frac{1}{2} \left\{ \mathcal{L}(0, \Lambda) - \Lambda \sum_{n=1}^{\infty} \beta_n \mathcal{I}(0, 2n-1) \right\}^{-1}, \quad (\text{A.6})$$

$$\begin{aligned} \beta_n + \Lambda \sum_{m=1}^{\infty} \beta_m \frac{4n+1}{2n+1} [\mathcal{I}(2n, 2m-1) - 2\mathcal{I}(2n, 1)\mathcal{I}(0, 2m-1)] \\ = \frac{4n+1}{2n+1} [\mathcal{L}(2n, \Lambda) - 2\mathcal{L}(0, \Lambda)\mathcal{I}(2n, 1)] \quad \text{for } n = 1, 2, \dots, \end{aligned} \quad (\text{A.7})$$

where

$$\begin{aligned} \mathcal{L}(\nu, \Lambda) &= -\mathcal{I}(\nu, 0) (1 + \Lambda) \\ &\quad + \Lambda \sum_{m=1}^{\infty} \frac{(-\Lambda)^m}{(m-1)!} \left[\Psi(n) + i\pi - \ln \Lambda - \frac{1}{m} \right] \mathcal{I}(\nu, m) - \frac{\partial \mathcal{I}}{\partial \sigma} \bigg|_{\substack{\nu=\nu \\ \sigma=m}}. \end{aligned} \quad (\text{A.8})$$

Equation (A.1) simplifies to

$$a_s^* = 1.74 - \frac{\pi}{2} \Lambda \ln \Lambda + \mathcal{O}(\Lambda) \quad \text{and} \quad b_s^* = \frac{\pi^2}{2} \Lambda + \mathcal{O}(\Lambda^2), \quad (\text{A.9})$$

when Λ approaches zero, and to

$$a_s^* = \frac{\pi}{3} - \frac{\pi}{8} \frac{1}{\Lambda} + \mathcal{O}(\Lambda^{-1}) \quad \text{and} \quad b_s^* = \frac{9\pi}{\Lambda^4} + \mathcal{O}(\Lambda^{-4}), \quad (\text{A.10})$$

when $\Lambda \rightarrow \infty$. Figure A1 shows the variations of a_s^* and b_s^* as a function of Λ .

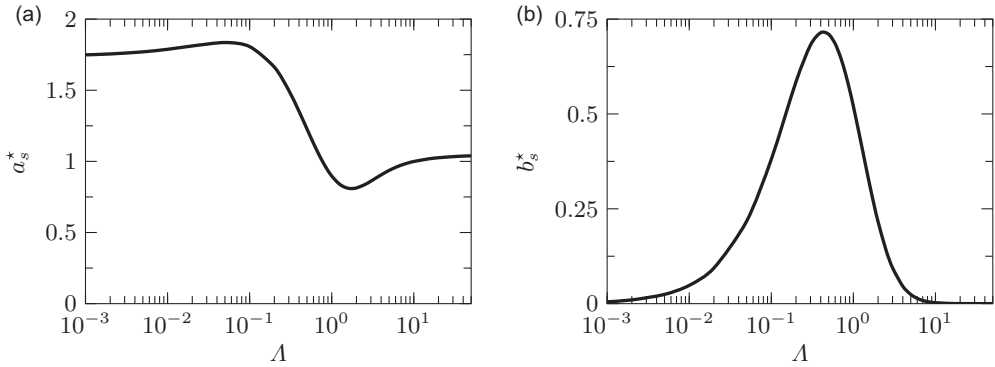


Figure A1. Plots of dimensionless (a) added mass and (b) radiation damping of the sphere (denoted by a_s^* and b_s^* , respectively) versus the dimensionless angular wavenumber Λ .

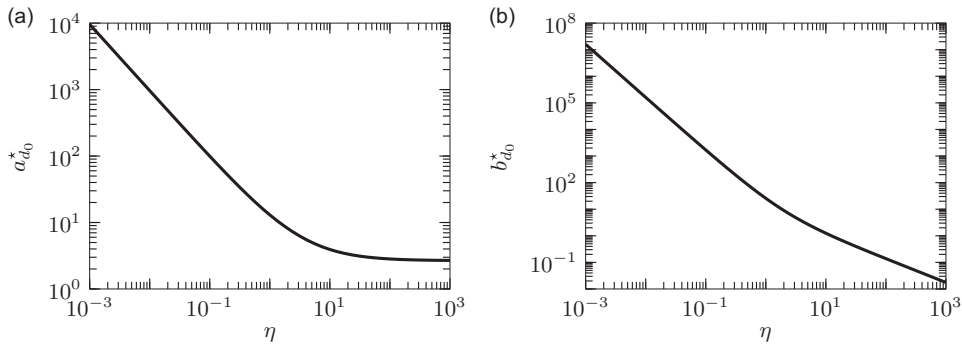


Figure B1. Plots of dimensionless (a) added mass and (b) viscous damping coefficients of a deeply submerged solid disk (denoted by $a_{d_0}^*$ and $b_{d_0}^*$, respectively) versus the dimensionless frequency (also known as the square root of the oscillatory Reynolds number) η .

Appendix B. Added mass and viscous damping coefficients of an oscillating annular disk

Zhang & Stone (1998) showed that the added mass a_{d_0} and viscous damping b_{d_0} coefficients of a deeply submerged solid disk oscillating with small amplitude can be obtained from

$$\frac{a_{d_0}}{\rho R_d^3} - i \frac{b_{d_0}}{\rho R_d^3 \omega} = a_{d_0}^* - i b_{d_0}^* = 8 \alpha_0, \quad (\text{B.1})$$

with R_d being the radius of the disk and

$$\sum_{m=0}^{\infty} \alpha_m \int_0^{\infty} k \left(1 - \frac{k}{\sqrt{k^2 + i \eta^2}} \right) J_{2m+1/2}(k) J_{2n+1/2}(k) dk = \delta_{0n} \quad \text{for } n = 0, 1, \dots, \quad (\text{B.2})$$

where m and n are integers, $\eta = \sqrt{\rho R_d^2 \omega / \mu}$, μ is the water viscosity, J is the Bessel function of the first kind and δ_{ij} is the Kronecker delta function. The hydrodynamics coefficients of the disk can be expressed succinctly as

$$a_{d_0}^* = \frac{64 \sqrt{2}}{3\pi \eta} + \dots \quad \text{and} \quad b_{d_0}^* = \frac{16}{\eta^2} + \frac{64 \sqrt{2}}{3\pi \eta} + \dots, \quad (\text{B.3})$$

in the asymptotic limit of $\eta \rightarrow 0$, and, according to Usman & Masoud (2025), as

$$a_{d_0}^* = \frac{8}{3} + \frac{\mathcal{A}_a \ln \eta + \mathcal{B}_a}{\eta} + \dots \quad \text{and} \quad b_{d_0}^* = \frac{\mathcal{A}_b \ln \eta + \mathcal{B}_b}{\eta} + \dots, \quad (\text{B.4})$$

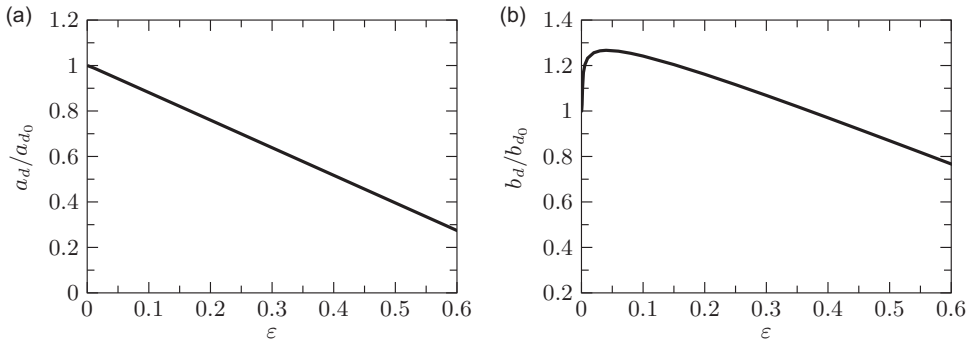


Figure B2. Plots of normalised (a) added mass and (b) viscous damping coefficients of a deeply submerged annular disk (i.e. a_d/a_{d0} and b_d/b_{d0} , respectively) versus the ratio of disk's inner to outer radius (denoted by ε) at $\eta = 10^3$.

in the opposite limit of $\eta \rightarrow \infty$, with

$$\mathcal{A}_a = 1.700, \quad \mathcal{B}_a = 8.349, \quad \mathcal{A}_b = 1.235, \quad \mathcal{B}_b = 8.155. \quad (\text{B.5})$$

Figure B1 shows the variations of a_d^* and b_d^* as a function of η .

Very recently, Usman & Masoud (2025) derived the following approximate expression for the added mass and viscous damping coefficients of an annular disk with an inner to outer radii ratio of $\varepsilon = R_p/R_d$

$$\frac{a_d}{\rho R_d^3} - i \frac{b_d}{\rho R_d^3 \omega} = a_d^* - i b_d^* = a_{d0}^* - i b_{d0}^* + 8p^{*2} \beta_0 \varepsilon, \quad (\text{B.6})$$

where

$$p^* = \frac{2i}{\sqrt{\pi}} \sum_{m=0}^{\infty} \frac{\Gamma(m+1)}{\Gamma(m+1/2)} \alpha_m, \quad (\text{B.7})$$

$$\sum_{m=0}^{\infty} \beta_m \int_0^{\infty} \frac{J_{2m+1/2}(k) J_{2n+1/2}(k)}{k \left(1 - \frac{k}{\sqrt{k^2 + i \varepsilon^2 \eta^2}} \right)} dk = \delta_{0n} \quad \text{for } n = 0, 1, \dots \quad (\text{B.8})$$

Equation (B.6) was obtained by applying the reciprocal theorem (Masoud & Stone, 2019) in conjunction with perturbation expansion in terms of the inner radius of the annular disk. From comparison with direct numerical simulations, it was shown that (B.6) maintains excellent accuracy over the range $0 \leq \varepsilon \leq 0.5$. Figure B2 presents the variations of a_d/a_{d0} and b_d/b_{d0} as a function of ε for $\eta = 10^3$.

Appendix C. Dimensionless representations of \bar{P}_{max} , $|X_r|$ and b_{pto}

The equations below provide non-dimensional forms of the quantities plotted in figures 2–3, 4 and 5, expressed in terms of the dimensionless parameters introduced here and in the previous two appendices. These formulations aid in rationalising the trends discussed in § 3

$$\begin{aligned} \bar{P}_{max}^{res,*} &= \frac{\bar{P}_{max}^{res}}{Q(\lambda/2\pi)} \\ &= 2 \left\{ 1 + \left(\frac{R_d}{R_s} \right)^{-3} \left(\frac{b_d^*}{b_s^*} \right) \left[\frac{b_s^{*2} + (m_s^* + a_s^* - \pi/\Lambda)^2}{b_d^{*2} + (m_d^* + a_d^*)^2} \right] \left[1 + \frac{|Z_i|}{\text{Re}(Z_i)} \right] \right\}^{-1}, \end{aligned} \quad (\text{C.1})$$

$$|X_r^*| = \left| \frac{X_r}{A} \right| = \left\{ \left(\frac{\Lambda^3}{b_s^*} \right) \left[b_s^{*2} + (m_s^* + a_s^* - \pi/\Lambda)^2 \right] \left[1 + \frac{\text{Re}(Z_i)}{|Z_i|} \right] \right\}^{-1/2}, \quad (\text{C.2})$$

$$b_{pto}^* = \frac{b_{pto}}{\rho R_d^3 \omega} = \frac{|Z_s^*| |Z_d^*|}{|Z_s^* + (R_d/R_s)^3 Z_d^*|}$$

$$= \sqrt{\frac{\left[b_s^{*2} + (m_s^* + a_s^* - \pi/\Lambda)^2 \right] \left[b_d^{*2} + (m_d^* + a_d^*)^2 \right]}{\left[b_s^* + (R_d/R_s)^3 b_d^* \right]^2 + \left[(m_s^* + a_s^* - \pi/\Lambda) + (R_d/R_s)^3 (m_d^* + a_d^*) \right]^2}}, \quad (\text{C.3})$$

where

$$Z_s^* = \frac{Z_s}{\rho R_s^3 \omega}, \quad Z_d^* = \frac{Z_d}{\rho R_d^3 \omega}, \quad m_s^* = \frac{m_s}{\rho R_s^3}, \quad m_d^* = \frac{m_d}{\rho R_d^3},$$

$$\frac{|Z_i|}{\text{Re}(Z_i)} = \sqrt{1 + \left\{ \frac{\left(m_d^* + a_d^* \right) + \left[\frac{b_d^{*2} + (m_d^* + a_d^*)^2}{b_s^{*2} + (m_s^* + a_s^* - \pi/\Lambda)^2} \right] (m_s^* + a_s^* - \pi/\Lambda) (R_d/R_s)^3}{b_d^* + \left[\frac{b_d^{*2} + (m_d^* + a_d^*)^2}{b_s^{*2} + (m_s^* + a_s^* - \pi/\Lambda)^2} \right] \left[b_s^* (R_d/R_s)^3 \right]} \right\}^2}. \quad (\text{C.4})$$

References

- Beatty, S. J., Hall, M., Buckham, B. J., Wild, P., & Bocking, B. (2015). Experimental and numerical comparisons of self-reacting point absorber wave energy converters in regular waves. *Ocean Engineering*, 104, 370–386.
- Clemente, D., Rosa-Santos, P., & Taveira-Pinto, F. (2021). On the potential synergies and applications of wave energy converters: A review. *Renewable and Sustainable Energy Reviews*, 135, 110162.
- Drew, B., Plummer, A. R., & Sahinkaya, M. N. (2009). A review of wave energy converter technology. *Proceedings of the Institution of Mechanical Engineers, Part A: Journal of Power and Energy*, 223(8), 887–902.
- Esmailzadeh, S., & Alam, M.-R. (2019). Shape optimization of wave energy converters for broadband directional incident waves. *Ocean Engineering*, 174, 186–200.
- Falcao, A. F. (2010). Wave energy utilization: A review of the technologies. *Renewable and Sustainable Energy Reviews*, 14(3), 899–918.
- Falnes, J. (1999). Wave-energy conversion through relative motion between two single-mode oscillating bodies. *Journal of Offshore Mechanics and Arctic Engineering*, 121(1), 32–38.
- Falnes, J. (2002). *Ocean waves and oscillating systems: Linear interactions including wave-energy extraction*. Cambridge University Press.
- Garcia-Teruel, A., & Forehand, D. I. M. (2021). A review of geometry optimisation of wave energy converters. *Renewable and Sustainable Energy Reviews*, 139, 110593.
- Goggins, J., & Finnegan, W. (2014). Shape optimisation of floating wave energy converters for a specified wave energy spectrum. *Renewable Energy*, 71, 208–220.
- Guo, B., & Ringwood, J. V. (2021a). Geometric optimisation of wave energy conversion devices: A survey. *Applied Energy*, 297, 117100.
- Guo, B., & Ringwood, J. V. (2021b). A review of wave energy technology from a research and commercial perspective. *IET Renewable Power Generation*, 15(14), 3065–3090.
- Guo, B., Wang, T., Jin, S., Duan, S., Yang, K., & Zhao, Y. (2022). A review of point absorber wave energy converters. *Journal of Marine Science and Engineering*, 10(10), 1534.
- Hamilton, A., Cazenave, F., Forbush, D., Coe, R. G., & Bacelli, G. (2021). The MBARI-WEC: A power source for ocean sensing. *Journal of Ocean Engineering and Marine Energy*, 7(2), 189–200.
- Hulme, A. (1982). The wave forces acting on a floating hemisphere undergoing forced periodic oscillations. *Journal of Fluid Mechanics*, 121, 443–463.
- Li, X., Martin, D., Jiang, B., Chen, S., Thiagarajan, K., Parker, R. G., & Zuo, L. (2021). Analysis and wave tank verification of the performance of point absorber wecs with different configurations. *IET Renewable Power Generation*, 15(14), 3309–3318.
- Liang, C., & Zuo, L. (2017). On the dynamics and design of a two-body wave energy converter. *Renewable Energy*, 101, 265–274.
- López, I., Andreu, J., Ceballos, S., De Alegría, I. M., & Kortabarria, I. (2013). Review of wave energy technologies and the necessary power-equipment. *Renewable and Sustainable Energy Reviews*, 27, 413–434.
- Masoud, H., & Stone, H. A. (2019). The reciprocal theorem in fluid dynamics and transport phenomena. *Journal of Fluid Mechanics*, 879, P1.

- Neary, V. S., Lawson, M., Previsic, M., Copping, A., Hallett, K. C., Labonte, A., Rieks, J., & Murray, D. (2014). Methodology for design and economic analysis of marine energy conversion (MEC) technologies (Tech. Rep., Sandia National Laboratories).
- Rosenberg, B. J., & Mundon, T. R. (2016). Numerical and physical modeling of a flexibly-connected two-body wave energy converter. In *Proceedings of the 4th marine energy technology symposium, Washington, DC*.
- Sheng, W. (2019). Wave energy conversion and hydrodynamics modelling technologies: A review. *Renewable and Sustainable Energy Reviews*, 109, 482–498.
- Soares, C. G., Bhattacharjee, J., Tello, M., & Pietra, L. (2012). Review and classification of wave energy converters. In *Maritime engineering and technology* (pp. 585–594). Taylor & Francis.
- Usman, M., & Masoud, H. (2025). Small-amplitude heave oscillations of an annular disk. *Journal of Fluid Mechanics*, 1017, A21.
- Wu, B., Wang, X., Diao, X., Peng, W., & Zhang, Y. (2014). Response and conversion efficiency of two degrees of freedom wave energy device. *Ocean Engineering*, 76, 10–20.
- Zhang, W., & Stone, H. A. (1998). Oscillatory motions of circular disks and nearly spherical particles in viscous flows. *Journal of Fluid Mechanics*, 367, 329–358.